remote sensing

MDPI

Article

Coseismic Deformation, Fault Slip Distribution, and Coulomb Stress Perturbation of the 2023 Türkiye-Syria Earthquake Doublet Based on SAR Offset Tracking

Wan Wang [1,2], Yunhua Liu [1,*], Xiaoran Fan [1], Chao Ma [2] and Xinjian Shan [1]

[1] State Key Laboratory of Earthquake Dynamics, Institute of Geology, China Earthquake Administration, Beijing 100029, China; wangw@ies.ac.cn (W.W.); fbb1108@ies.ac.cn (X.F.); xjshan@163.com (X.S.)
[2] School of Surveying and Land Information Engineering, Henan Polytechnic University, Jiaozuo 454003, China; mac@hpu.edu.cn
* Correspondence: liuyunhua@ies.ac.cn; Tel.: +86-(10)-62009346

Abstract: The Türkiye-Syria earthquake doublet of 6 February 2023 (Mw 7.8 at 01:17 UTC and Mw 7.6 at 10:24 UTC) resulted in extensive damage and tens of thousands of casualties. We present the surface displacements of the two earthquakes from synthetic aperture radar (SAR) offset tracking measurements. We extracted the geometric parameters of the rupture faults from the surface displacements and early aftershock distribution, based on which we inverted the coseismic slip distributions. We then calculated Coulomb stress to investigate the triggering relationship between the earthquakes and stress transfer to neighbouring faults and regions. The coseismic ruptures of the earthquake doublet were predominantly left-lateral strike-slip motions distributed between 0 and 15 km depth. The maximum fault slip reached > 8 m (Mw 7.8) and almost 10 m (Mw 7.6). The coseismic deformation and fault slip motion are consistent with the overall westward extrusion of the Anatolian Plate relative to the Eurasian and Arabian plates. The Mw 7.8 earthquake increased Coulomb failure stress at the hypocenter of the Mw 7.6 earthquake, implying that the Mw 7.8 event had a strong positive causative effect. Moreover, coseismic stress perturbations revealed a positive Coulomb stress effect on the middle Puturge Fault, northern Dead Sea Fault Zone (DSFZ), Yesemek Fault, Antakya Fault, and Turkoglu Fault, indicating an increasing seismic hazard in these regions.

Keywords: 2023 Türkiye-Syria earthquake doublet; East Anatolian Fault Zone; SAR offset tracking; fault slip distribution; Coulomb stress changes

Citation: Wang, W.; Liu, Y.; Fan, X.; Ma, C.; Shan, X. Coseismic Deformation, Fault Slip Distribution, and Coulomb Stress Perturbation of the 2023 Türkiye-Syria Earthquake Doublet Based on SAR Offset Tracking. *Remote Sens.* **2023**, *15*, 5443. https://doi.org/10.3390/rs15235443

Academic Editor: Alex Hay-Man Ng

Received: 10 September 2023
Revised: 19 October 2023
Accepted: 26 October 2023
Published: 21 November 2023

1. Introduction

A destructive earthquake doublet struck Türkiye and northern Syria on 6 February 2023. The powerful mainshock (Mw 7.8 at 01:17 UTC) triggered a series of aftershocks, including a magnitude Mw 7.6 earthquake that occurred ~9 h later at a distance of 95 km from the Mw 7.8 event. These events caused widespread damage and tens of thousands of casualties [1]. The Mw 7.8 earthquake initiated on the Narh Fault (NF) [2,3] and then ruptured bilaterally along the East Anatolian Fault Zone (EAFZ). The Mw 7.6 earthquake mainly occurred on the Cardak Fault (CF) and propagated bilaterally along the east-west direction [4–6]. The occurrence of two such large earthquakes (Mw > 7.5) on nearby faults within a few hours of each other is very rare.

This event follows a number of large earthquakes that occurred along the EAFZ in the 19th and 20th centuries, including the 1986 Mw 6.1, 2003 Mw 6.3, 2010 Mw 6.1, and 2020 Mw 6.8 earthquakes [7]. Most of these earthquakes occurred to the east of Erkenek [8]; in contrast, the fault to the west (the Pazarcık and Amanos segments) has been largely locked for more than a century and has accumulated a significant amount of energy.

Following the earthquake, comprehensive investigations have been undertaken to meticulously examine the rupture process and seismic tectonics of the twin earthquakes

in Türkiye. Melgar et al. [5] used high-rate GNSS (HR-GNSS) recordings and synthetic aperture radar (SAR) images to perform a joint finite fault inversion and analyse rupture processes and velocities for the Mw 7.8 event. They found that the 2023 Mw 7.8 earthquake occurred in two phases and that a secondary structure (the NF) dominated the rupture onset. In addition, they discussed the supershear rupture states of both the Mw 7.8 and 7.6 earthquakes. Barbot et al. [4] used geodetic and seismic data to estimate the peak sliding, slip deficit fraction, and spatio-temporal characteristics of aftershocks for the Mw 7.8 and 7.6 earthquakes. Jia et al. [9] used HR-GNSS and strong motion data to determine the complex rupture histories, including sub-shear and supershear events. They mainly emphasised the role of fault interactions and the necessity of heterogeneous background stresses. Meng et al. [10] used long-range and local seismic data, HR-GNSS records, and SAR images to perform a joint finite fault inversion by means of slow-enhanced backpropagation in order to explore the rupture process of the Mw 7.8 earthquake. Through differential interferometric SAR (D-InSAR) processing of the 2023 Türkiye-Syria earthquake sequence, Mila et al. [11] provided an initial reference for ground deformation. Li et al. [12] analysed the surface displacement, co-seismic slip distribution, inter-seismic fault slip rates, locking depths, static Coulomb damage stress changes, and fault geometry using SAR images and Global Positioning System (GPS) data. An et al. [13] combined optical and SAR images to generate three-dimensional (3D) deformation fields for the two seismic events and focused on assessing the surface deformation.

These studies provide important constraints and account for the specificity of the 2023 earthquake sequence. However, further near-field observations are needed to refine the slip distribution, stress-triggering relationship between the earthquakes, and regional stress perturbations [14]. Moreover, analysing stress accumulation within this fault zone is needed to better understand the sequence of strong seismic activity and seismic hazards in the region. In this study, we used SAR data processed by pixel offset tracking technology to derive two-dimensional (2D) displacements of the 2023 Türkiye-Syria earthquake doublet (Figure 1). By analysing changes in displacements, we obtained the geometric characteristics and deformation magnitudes of the rupture faults. Then, we inverted the coseismic slip distribution of the earthquake sequence based on the homogeneous elastic half-space dislocation model. Finally, we analysed the fault motion, rupture patterns, and stress transfer. The results of this study provide new insights into the mechanisms of strong earthquakes and inter-plate motion in the EAFZ.

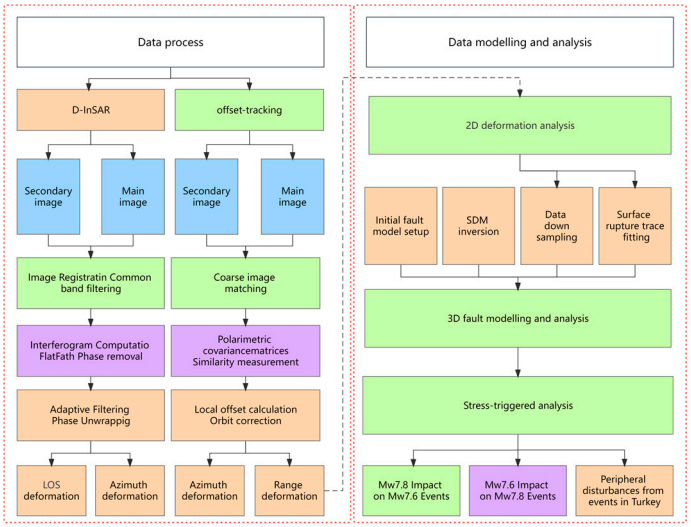

Figure 1. A workflow was used to study the 2023 Türkiye-Syria earthquake sequence. LOS deformation, line-of-sight deformation.

2. Materials and Methods

2.1. Tectonic Setting

The first event, which occurred at 01:17 UTC on 6 February 2023, had a magnitude of Mw 7.8, an epicentre located at 37.17°N and 37.03°E, and a focal depth of ~10 km (Table 1; https://earthquake.usgs.gov/, accessed on 20 February 2023). This powerful mainshock triggered a series of aftershocks, including a magnitude Mw 7.6 earthquake that occurred ~9 h later at a distance of 95 km from the Mw 7.8 event. Focal mechanism solutions indicate that the earthquake doublet was dominated by left-lateral strike-slip motion. The Mw 7.8 earthquake initiated on the NF [2,3] and then ruptured bilaterally along the EAFZ, consisting of two to four sub-events with a total duration of 20–80 s [8]. The Mw 7.6 earthquake mainly occurred on the Cardak Fault (CF) and propagated bilaterally along the east-west direction [4–6].

Table 1. Focal mechanism solutions for the 2023 Mw 7.8 Türkiye-Syria earthquake.

Orbit	Track	Azimuth Angle (°)	Incidence Angle (°)	Reference Image	Secondary Image
Ascending	T14	−22	39	28 January 2023	9 February 2023
	T116	−22	39	4 February 2023	28 February 2023
Descending	T21	−103	39	29 January 2023	10 February 2023

In terms of regional tectonics, the epicentral region is located near the triple junction of the Anatolian, Arabian, and Eurasian plates [11,12,15,16] (Figure 2). The Anatolian Plate, which lies between the other two plates, shows extrusive movement towards the Aegean Sea owing to the northward movement of the Arabian and Eurasian plates [4,17,18]. The active structures of Anatolia consist of the North Anatolian Fault Zone (NAFZ) and the EAFZ. As the boundary between the Anatolian and Eurasian plates, the NAFZ is dominated by left-lateral strike-slip motion [19]. Together with the EAFZ, it accommodates the counterclockwise movement of the Anatolian Plate towards the west. The EAFZ intersects the NAFZ at the Karliova triple junction and then extends southwestwards ~600 km to the Kahramanmaras triple junction near Antakya, where it joins the Dead Sea Fault Zone (DSFZ) [20]. The EAFZ mainly connects seven segments: Karlıova, Ilıca, Palu, Puturge, Erkenek, Pazarcık, and Amanos [20,21]. Slip rates vary across these fault zones owing to the influence of conjugate fractures, pullout basins, and their discontinuous nature. GPS and geological slip rates are consistent between the Karlıova and Puturge segments (8.3 mm/a) [22–24]. Influenced by the valley geomorphology, the slip rate of the Erkenek segment is ~6.5–7.0 mm/a [20]. The slip rate of the Pazarcık segment is more controversial: Westaway et al. [25] obtained a slip rate of 4.0–4.6 mm/a by considering the influence of serpentinite and drainage channel offsets; Karabacak et al. [26] found a slip rate of 9.18 mm/a based on paleoseismological data. Through radiometric dating of Quaternary volcanic rocks with serpentinite offsets in the vicinity of this section and GPS data of the lateral motion of the Arabian and African plates, Duman and Emre [20] calculated a slip rate of 5.57 mm/a for the Amano segment. Variable geological features and discontinuities between faults not only increase the complexity of the EAFZ but also have a controlling effect on the rupture locations of large earthquakes.

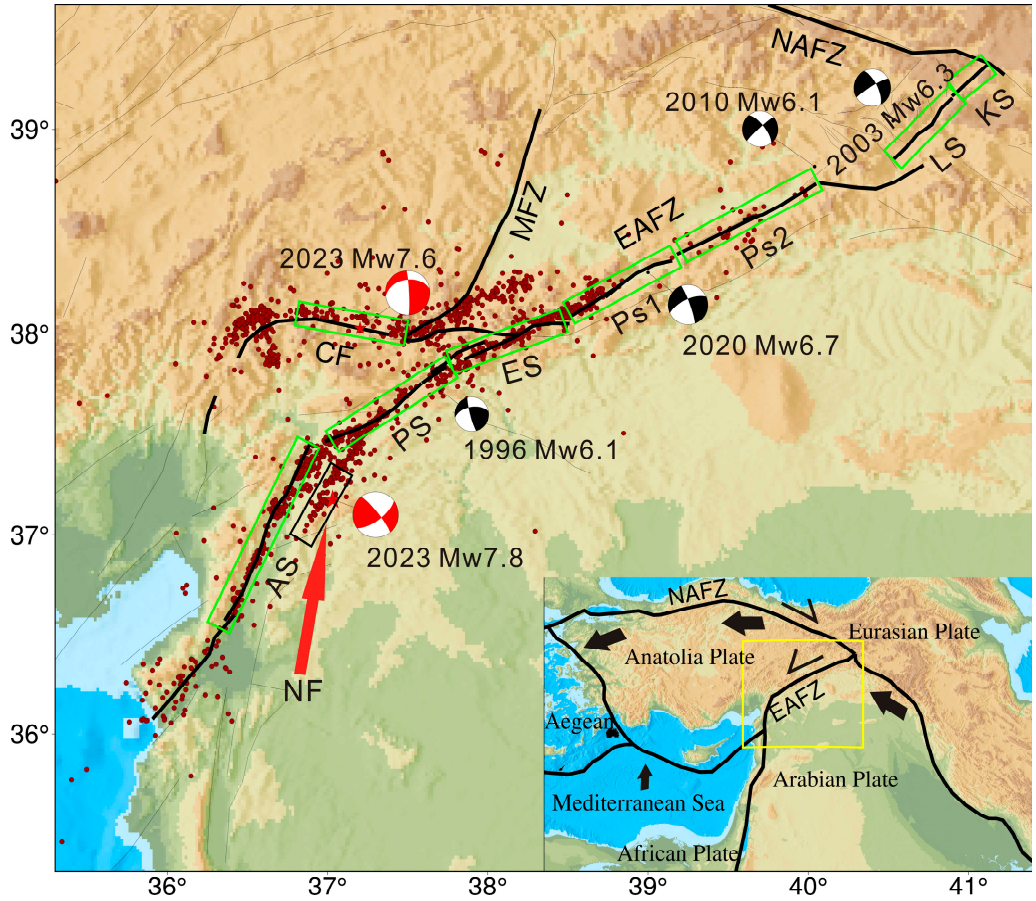

Figure 2. Tectonic setting of the 2023 Türkiye-Syria earthquake sequence. Red beach balls indicate the 2023 Mw 7.8 and 7.6 earthquakes on 6 February 2023. The yellow box denotes the study area. Black beach balls represent strong historical earthquakes along the EAFZ. Red stars represent the epicentres of the 2023 Mw 7.8 and 7.6 earthquakes. Green rectangular boxes represent the main active faults. The black rectangular box represents the Narh Fault [10]. The aftershock distributions of the 2023 Türkiye-Syria earthquake sequence are derived from Lomax [27]. The inset shows the motions of major tectonic units [28]. Abbreviations: EAFZ: East Anatolian Fault Zone, NAFZ: North Anatolian Fault Zone, MFZ: Malatya Fault Zone, AS: Amanos Fault, PS: Pazarcık Fault, ES: Erkenek Fault, Ps1: Puturge Fault, Ps2: Palu Fault, LS: Ilıca Fault, KS: Karlıova Fault, CF: Cardak Fault, NF: Narh Fault.

2.2. Data Collection and Analysis

Surface displacement, a direct manifestation of earthquakes, plays a pivotal role in earthquake hazard assessment, fault slip modelling, and understanding triggering mechanisms [29,30]. SAR, a remote sensing technology, effectively captures high-precision, high-spatial-resolution surface displacement fields by transmitting radar pulses to the ground and measuring the amplitude and phase of the reflected signals [31,32]. For a pair of SAR images, based on the phase information, D-InSAR [33] methods have been extensively employed for monitoring surface deformation resulting from moderate to strong earthquakes in recent years [34–37]. Additionally, SAR amplitude information enables the pixel tracking method [38], simulating the acquisition of surface displacements in both the line-of-sight (LOS) and azimuth (AZ) directions of the satellite. Notably, when the ground displacement exceeds half of a pixel's interference fringe, the offset tracking method serves as a valuable interferometric synthetic aperture radar (InSAR) complement [39,40]. Building on this foundation, we aimed to investigate the 2023 Türkiye-Syria earthquake sequence by employing two distinct methodologies: D-InSAR and SAR offset tracking.

The InSAR dataset in this study consisted of six SAR acquisitions. For ascending track T014, the master and slave images were acquired on 28 January 2023 and 9 February 2023 (gap of 12 days). For ascending track T116, the master and slave images were acquired on 4 February 2023 and 28 February 2023. For descending track T21, we chose image pairs on 29 January 2023 and 10 February 2023. The detailed parameters of the S1A data are shown in Table 2.

Table 2. Basic parameters of coseismic synthetic aperture radar (SAR) data of the 2023 Türkiye-Syria earthquake sequence.

Orbit	Track	Azimuth Angle (°)	Incidence Angle (°)	Reference Image	Secondary Image
Ascending	T14	−22	39	28 January 2023	9 February 2023
	T116	−22	39	4 February 2023	28 February 2023
Descending	T21	−103	39	29 January 2023	10 February 2023

By processing the available S1A Single Look Complex (SLC) images, we generated three D-InSAR interferograms using the GAMMA package with multi-look factors of 2 and 10 in the azimuth and range directions, respectively [41]. A 3-arc-second Shuttle Radar Topography Mission (SRTM) digital elevation model (DEM) was used to remove topographical effects. The interferograms were then filtered using a power spectrum method [42], followed by unwrapping with the minimum cost flow algorithm [43]. Finally, the unwrapped interferograms were geocoded into geodetic coordinates (Figure 3).

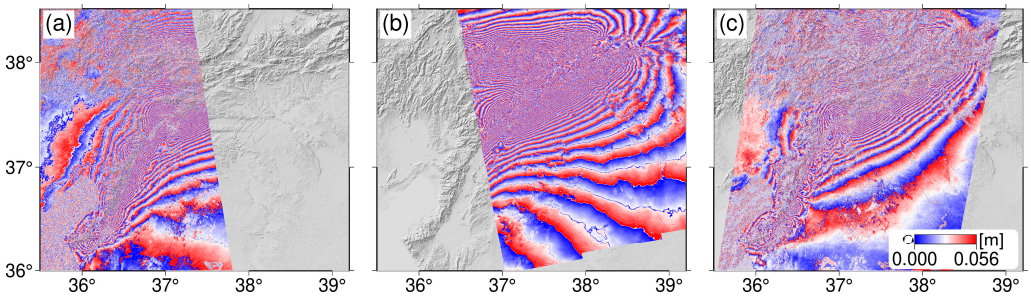

Figure 3. Interferograms of the 2023 Turkey sequence. (**a**) Interferogram of ascending track T14 based on the differential interferometric synthetic aperture radar (D-InSAR) method. (**b**) Interferogram for ascending track T116 based on the D-InSAR method. (**c**) Interferogram for descending track T21 based on the D-InSAR method.

The unwrapping results suffered from many fringes and areas of decorrelation. The reasons for this included: (1) large deformation gradients in the source region, with phase differences between adjacent elements in the centre of the deformation region exceeding π (i.e., 1/2 period) and coherence that was often very low or even completely out of phase [37,44]; (2) the double shock and medium-intensity aftershock occurring in a short period of time led to deconvolution failure. Multiple earthquakes cause phases to overlap, and existing algorithms have difficulty distinguishing the overlapping phases or interference fringes [45]. Therefore, the D-InSAR results of the Sentinel data were not analysed or adopted in the source modelling.

The pixel offset tracking technique uses the amplitude information of SAR images to compute ground displacements in both azimuth and range directions [12,46,47]. This method is unaffected by phase coherence and phase unwrapping [48,49]. It was therefore particularly suitable for the 2023 Türkiye-Syria seismic sequence. We first aligned the images to the pre- and post-earthquake data, and then the single-look SAR images were segmented into smaller blocks. We selected a search window of 64 × 192 pixels (range × azimuth) to calculate the offset between the corresponding blocks using the intensity

correlation method. Finally, we converted the estimated offsets into displacements in both the azimuth and range directions.

3. Results

3.1. Offset Deformation Results

Using pixel offset tracking analysis, we measured ground displacements in the vicinity of the fault traces [50]. The most notable features were the sharp discontinuities for both events.

For the Mw 7.8 earthquake, the location of the surface rupture zone was mainly concentrated on the southern branch of the EAFZ. The coseismic deformation patterns in the ascending displacement fields (T14 and T116) were basically the same, while the descending displacement field showed a diametrically opposite deformation pattern (T21) (Figure 4a–c): positive (negative) displacement was seen in descending (ascending) deformation maps for the north-wall of the fault, suggesting that the earthquakes generated deformation mainly in the horizontal direction, which is consistent with the characteristics of strike-slip earthquakes. Moreover, this is in agreement with the focal mechanism from the Global Centroid-Moment-Tensor (GCMT). To the southwest of the Mw 7.8 event, the rupture trace could be fitted based on the T121 displacement gradient; to the northeast, the rupture trace was mainly fitted based on the T116 displacement gradient. According to seismic wave data and the 24-h post-earthquake aftershock distribution, the dashed line in Figure 4a represents the original rupture fault of the earthquake.

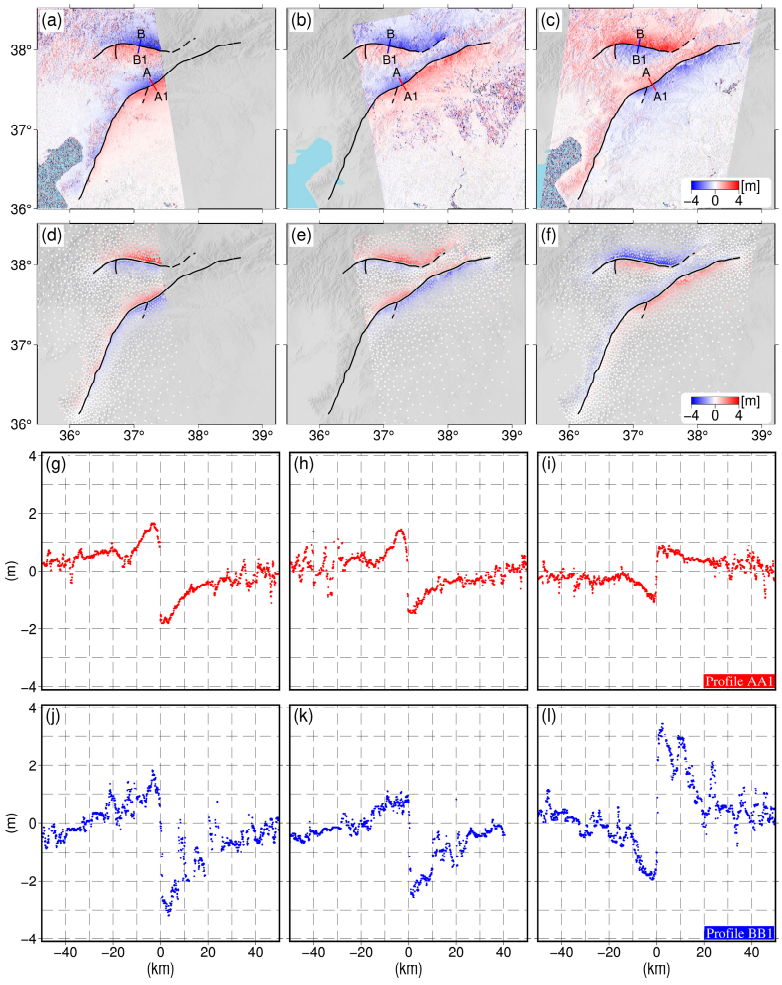

Figure 4. (**a**–**c**) Coseismic deformation of the 2023 Türkiye-Syria seismic sequence along the range direction for ascending tracks T14 and T116 and descending track T21. Black lines represent fault rupture traces based on surface deformation. (**d**–**f**) Downsampled points for ascending tracks T14

and T116 and descending track T21. (**g**–**i**) Profiles of ascending tracks T14 and T116 and descending track T21 (red, AA1 profile). (**j**–**k**) Profiles of ascending tracks T14 and T116 and descending track T21 (blue, BB1 profile). AA1 indicates a 30 km long by 0.1 km wide section line along the southern branch of the EAFZ (the main rupture zone of the Mw 7.8 earthquake rupture), and BB1 indicates a 30 km long by 0.1 km wide section line along the northern branch of the EAFZ (the main rupture zone of the Mw 7.6 earthquake rupture).

For the Mw 7.6 earthquake, the surface rupture zone was mainly located on the Carkdak Fault, which is the northern branch of the EAFZ. The T21 displacement gradient showed a distinct vertical branch to the west of the event. We identified the rupture northeast of the Mw 7.6 event from the spatial distributions of aftershocks (Figure 1).

To better define the surface rupture characteristics of the Türkiye-Syria earthquake sequence, we took a profile 30 km long and 0.1 km wide perpendicular to the fault strike (Figure 4h,i), centred on the identified rupture trace (Figure 4c). The ascending displacement range was greater than the descending displacement range. For ascending displacement during the Mw 7.8 earthquake, profiles AA1 and BB1 showed displacements of 5 and 3.5 m (T14) and 2.9 and 3.3 m (T116), respectively (Table 3). In contrast, for the same position on the descending track (T21), deformation was only 2.0 and 5.3 m.

Table 3. Seismic sequence profile line variables of the 2023 Türkiye-Syria seismic sequence. AA1 is located on the southern branch of the East Anatolian Fault Zone (EAFZ), and BB1 is located on the northern branch of the EAFZ. The exact locations are shown in Figure 4a.

Track Profile	ASCT14		ASCT16		DSCT21	
	AA1	**BB1**	**AA1**	**BB1**	**AA1**	**BB1**
max (m)	1.8	1.7	1.4	0.9	0.9	3.4
min (m)	−3.2	−1.8	−1.5	−2.4	−1.1	−1.9

3.2. Fault Model and Slip Distribution Inversion

3.2.1. Rupture Trace Fitting

In this study, we first combined the gradient of the displacement field with the spatial distribution of aftershocks (as shown in Figure 2) to produce a fault trace with a SW-NE strike for the Mw 7.8 event and an east-west strike for the Mw 7.6 event (black lines in Figure 4c). The rupture trace of the south-west branch of the Mw 7.8 event was fitted mainly with reference to the displacement field of descending track T21, while the north-east branch was fitted mainly in combination with the displacement field of ascending track T116. Based on the results of Lomax et al. [27], the rupture started from the NF and then ruptured bilaterally along the EAFZ (represented as the dotted line in Figure 4a).

The rupture trace of the Mw 7.6 event was located on the Carkdak Fault and was fitted based on the deformation field. The branch rupture west of the Mw 7.6 event was fitted using the T21 deformation field. The rupture at the eastern end of the Carkdak Fault, which is parallel to the EAFZ, was fitted based on the spatial distribution of aftershocks.

3.2.2. Data Downsampling

Continuous deformation fields consist of hundreds of millions of points, which is computationally expensive and can lead to difficulty in convergence of the results owing to noise interference [50]. Therefore, before inversion, the deformation field data were downsampled using the Delaunay triangulation method [51]. This method retains more points in the region of large near-field deformation and gradually reduces the sampling points for far-field data, which ensures data quality and improves sampling efficiency. The final data set consisted of 8600 points (Figure 4d–f).

3.2.3. Constructing the Initial Fault Model

By comparing the results of the field geological study, seismological study, and offset and optical remote sensing image deformation fields, a three-segmented geometric fault surface rupture model (S1–S3) was established for the southern main branch of the EAFZ. In most places, this fault segmentation model is consistent with the surface rupture of the field geological survey of the Mw 7.8 earthquake, which started at NF. For the Mw 7.6 earthquake, we divided the Carkdak Fault into a two-fault segmentation model (S4, S5) according to changes in rupture strike; in addition, we also considered a small vertical fault branch Cf1 (black dashed branch to the left of profile BB1 in Figure 4c), which was observed by combining the distribution of aftershocks with the descending deformation field. Focal mechanism solutions provided by several organisations show that the dip is between 64° and 89°, and the rake angle varies between −1° and 11°. Most of the aftershocks were located at a depth of 20 km. Combining these parameters, we used a four-segment fault model for the Mw 7.8 event and a three-segment model for the Mw 7.6 event to invert the slip distributions. The lower boundary of the fault model was located at a depth of 30 km, and the rake angle was set to (−20°, 20°), taking into account that both ruptures were left-lateral strike-slip motions. The simulated fault for the Mw 7.8 earthquake extended from 36.14° E and 36.12°N (southwest point) to 38.67°E and 38.09°N (northeast point). The modelled fault for the Mw 7.6 earthquake extended from 36.36°E and 37.89°N (the western point) to 38.15°E and 38.24°N (the eastern point). Along the strike and depth directions, we discretised the fault surface into 4 × 4 km patches and constructed the fault model in an elastic and homogeneous half-space.

A linear inversion method, the Steepest Descent Method (SDM) [52], was used to invert the coseismic slip distribution of the Türkiye-Syria earthquake sequence. The mathematical formula for the inversion is:

$$F(x) = ||Gm(x) - y||^2 + \alpha^2||Hm||^2 \quad (1)$$

where G is the elastic half-space Green's function, $m(x)$ is the sliding vector matrix, H is the Laplace operator, y is the surface observation matrix, α is the smoothing factor, and Hm is the weighting factor of the associated displacement magnitude with the Laplace operator finite difference approximation, and is the roughness of the fault slip. In this inversion, the Green's function of the uniform elastic half-space model was calculated using the method described in Okada [53], assuming a Poisson's ratio of 0.25.

3.2.4. Coseismic Slip Distribution

The main rupture of the Mw 7.8 earthquake was located on the southern branch of EAFZ. Coseismic slip was concentrated at depths of 0–10 km and tapered off at depths of 11–15 km (Figure 5b). This is in accordance with the EAFZ being prone to shallow-source earthquakes [54]. Along the strike, coseismic slip was high in the centre and low on either side. The maximum rupture depths of the S1, S2, and S3 fault segments were 5.6, 8.4, and 7.1 m, corresponding to depth ranges of 0–5, 0–15, and 0–10 km, respectively. The rupture initiation bifurcation fault had a maximum slip of ~2.7 m. The coseismic slip on the Cardark Fault was mainly caused by the Mw 7.6 shock. The rupture depth ranged from 0 to 15 km, the average slip was 2.6 m, and the rake was 3.4°. The maximum slip was 9.6 m, which was concentrated on the western side of the source.

The total moment magnitude of the two earthquakes obtained from the inversion was Mw 7.9, which is higher than those of the GCMT and United States Geological Survey (USGS). This is probably because the coseismic deformation field includes the contribution of short-term deformation after the earthquake.

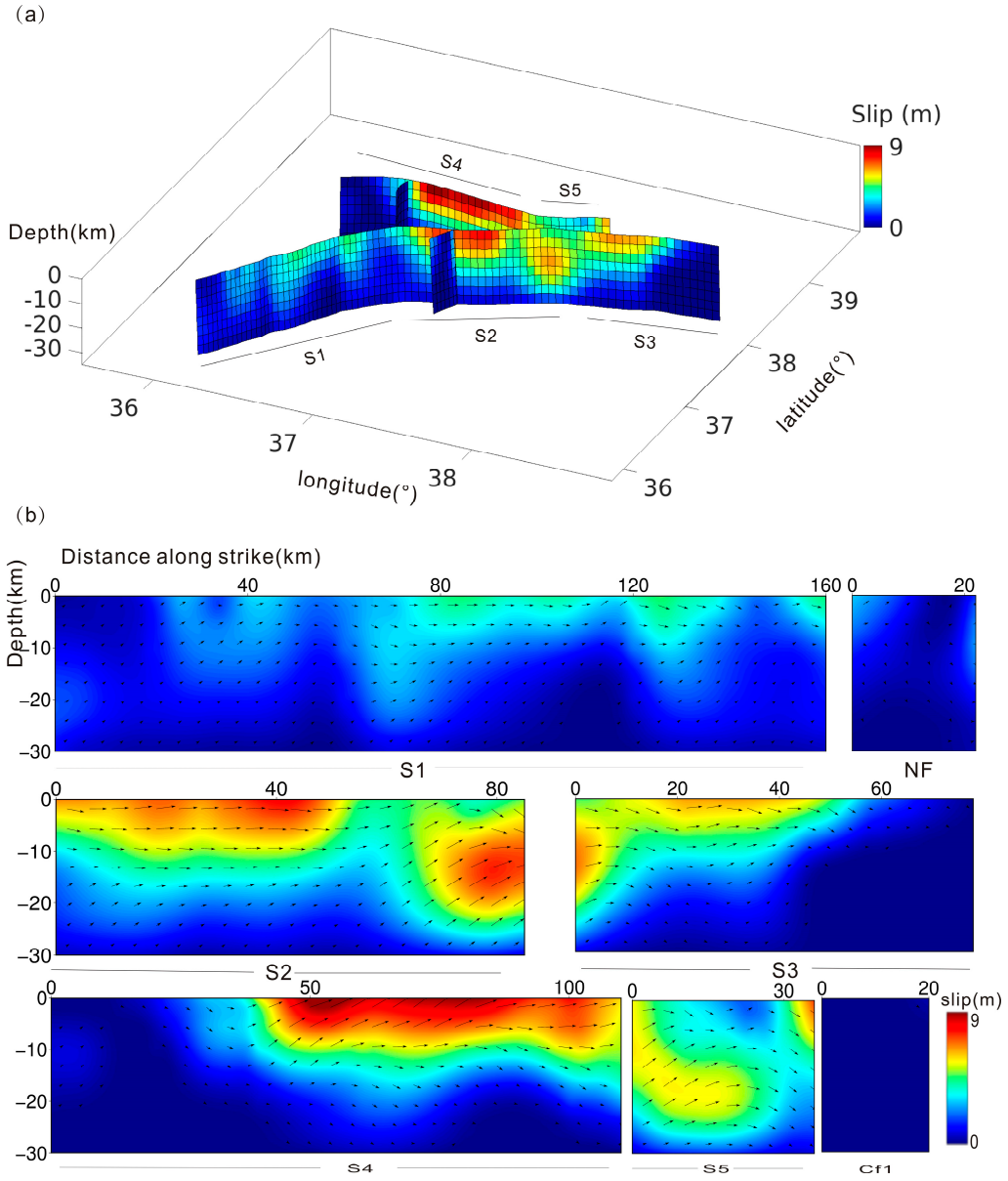

Figure 5. Rupture model of the 2023 Türkiye-Syria seismic sequence. (**a**) Three-dimensional (3D) rupture model of the 2023 Türkiye-Syria seismic sequence. Black solid line segments (S1–S5) indicate the segmented fault numbers used for inversion in the synthetic aperture radar (SAR) data. Colours denote the total slip magnitude (in metres); the red colour saturates at 9 m in S4 with a maximum slip of 9.6 m. (**b**) Two-dimensional (2D) distribution of cumulative coseismic fault slips.

The residuals between the observed and modelled results (Figure 6) suggest that simulated and observed displacements are in good agreement. However, we observed some significant discrepancies, particularly in the near-field of the fault, where the fault geometry and strike change. Moreover, sources of error can also include observational noise, inelastic deformation, and simplification of seismogenic faults [44].

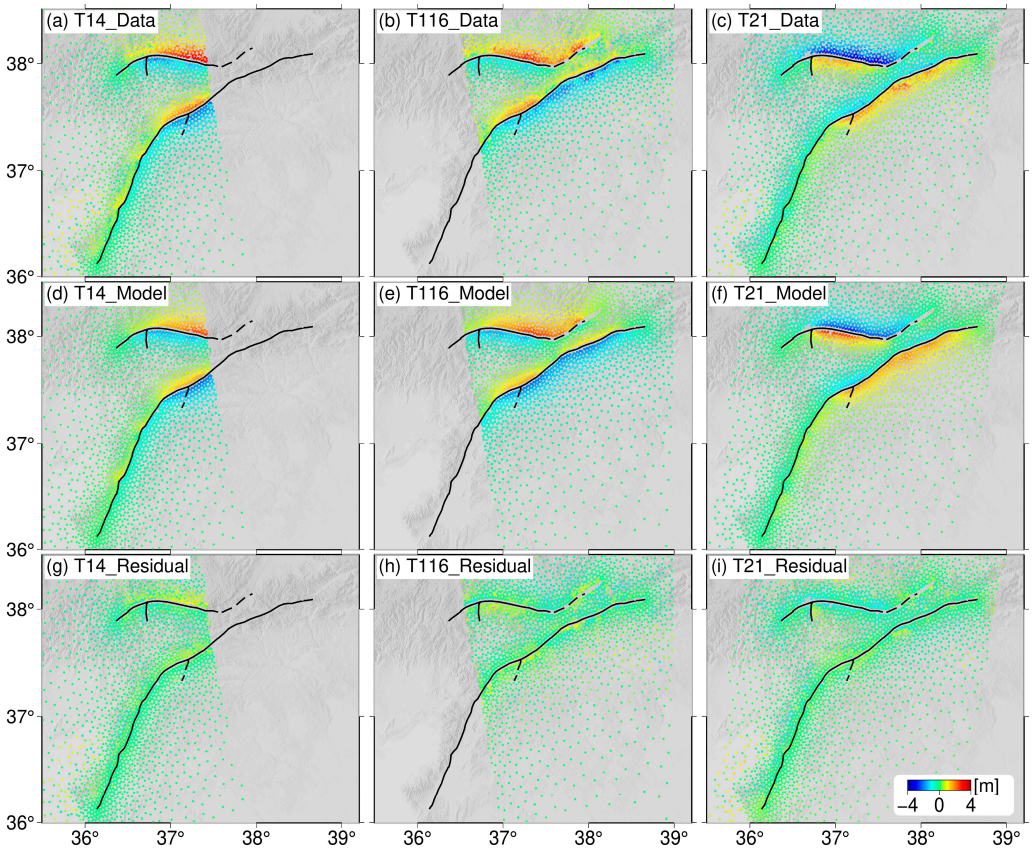

Figure 6. Observed and modelled parameters of the 2023 Türkiye-Syria earthquake sequence. (**a**–**c**) Synthetic aperture radar (SAR) observations for ascending ((**a**) T14, (**b**) T116) and descending ((**c**) T21) tracks. (**d**–**f**) SAR model calculations for ascending ((**d**) T14, (**e**) T116) and descending ((**f**) T21) tracks. (**g**–**i**) Residuals for ascending ((**g**) T14, (**h**) T116) and descending ((**i**) T21) tracks. Black lines denote surface rupture traces.

4. Discussion

4.1. Interaction between Plates

Both the Mw 7.8 and 7.6 earthquakes ruptured on faults of the EAFZ and exhibited left-lateral slip motion. Such an earthquake doublet, with two earthquakes rupturing nearby faults with almost identical rupture patterns, is rare. The most similar previous examples include the 2019 Mw 7.2 Ridgecrest earthquake and the 2012 Mw 8.6 Indian Ocean earthquake. For the 2023 Türkiye-Syria earthquake sequence, the identical movement patterns are inextricably linked to the westward motion of the Anatolian Plate. For the Mw 7.8 earthquake, the main faults that ruptured were EAFZ segments (Erkenek, Pazarcık, and Amanos). Influenced by the rapidly changing relative motions between the Anatolian and Arabian plates, these fault motions were mainly dominated by left-lateral strike-slip [15,54]. Relative movement between faults accelerated after the earthquakes. Moreover, the rupture motion of the Mw 7.6 earthquake was also dominated by left-lateral slip, which was precisely matched to the rightward motion of the Cardak Fault and the leftward motion of the EAFZ. These movements are consistent with the counterclockwise extrusion of the Anatolian Plate into the Aegean Sea.

4.2. Stress-Triggering Relationship between the Mw 7.8 and 7.6 Earthquakes

According to Coulomb failure law, when an earthquake occurs, it modulates the stress state of surrounding active ruptures, which in turn triggers or inhibits the seismic hazard

of ruptures in the vicinity [55,56]. Coulomb failure stress (∇CFS) is an important indicator of the probability of earthquake triggering:

$$\nabla CFS = \nabla\tau_s + \mu(\nabla\sigma_n + \nabla p) \quad (2)$$

where $\nabla\tau_s$ is the change in shear stress resolved in the slip direction of a fault that may fail in a subsequent earthquake, $\nabla\sigma_n$ is the change in normal stress due to the first earthquake perpendicular to the plane of the subsequent earthquake fault (positive for extension), ∇p is the change in pore pressure, and μ is the coefficient of friction, which is typically set to 0.4 for left-lateral strike-slip movement.

First, we used the distributed slip models of the EAFZ and NF faults to calculate the stress transferred by the Mw 7.8 mainshock. We set the rake angle to 0° to match the characteristics of a left-lateral strike-slip fault. As shown in Figure 7, the distribution of stresses generated by the Mw 7.8 earthquake on the EAFZ was the opposite of the slip distribution; that is, areas of high slip mainly show stress suppression, which corresponds to the distribution of stresses on the fault. The stress generated by the Mw 7.8 earthquake revealed a significant segmentation effect on the Cardak Fault. Stress was negative on the left of S4 but positive on the right, and completely negative for S5. The Mw 7.8 mainshock increased the Coulomb failure stress at the hypocenter of the Mw 7.6 shock to over 2 bar, increasing the probability of the second event (Figure 7a).

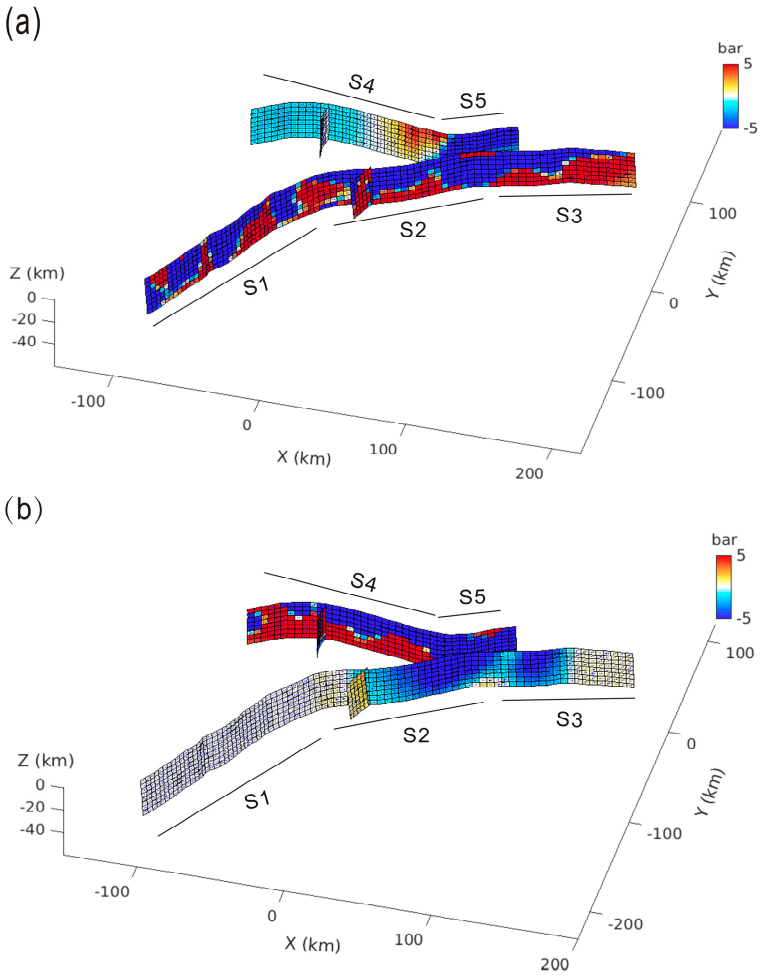

Figure 7. Stress transfer to surrounding faults by the two earthquakes of the 2023 Türkiye-Syria earthquake sequence. Black solid line segments (S1–S5) indicate the segmented fault numbers used for inversion in the synthetic aperture radar (SAR) data. the dots in the colored squares resprent represent grids, each of size 4 × 4 km. (**a**) Stress transfer to surrounding faults by the Mw 7.8 earthquake. (**b**) Stress

transfer to surrounding faults by the Mw 7.6 earthquake. As first described by Harris et al. [57], the blue region had the greatest fault slip, the lowest remaining stress, and the lowest future earthquake risk. In contrast, the red region, also known as the trigger zone, continues to experience high stress and a high risk of future earthquakes.

We then used the distributed slip model obtained from the Mw 7.6 earthquake to calculate stress on the EAFZ (Figure 7b). The majority of the energy in the Cardak Fault was released after the earthquake, and the stress caused by the Mw 7.6 earthquake had little effect on S1. However, significant negative stress changes were estimated along S2 and west of S3, corresponding to areas with small numbers of aftershocks (as shown in Figure 8).

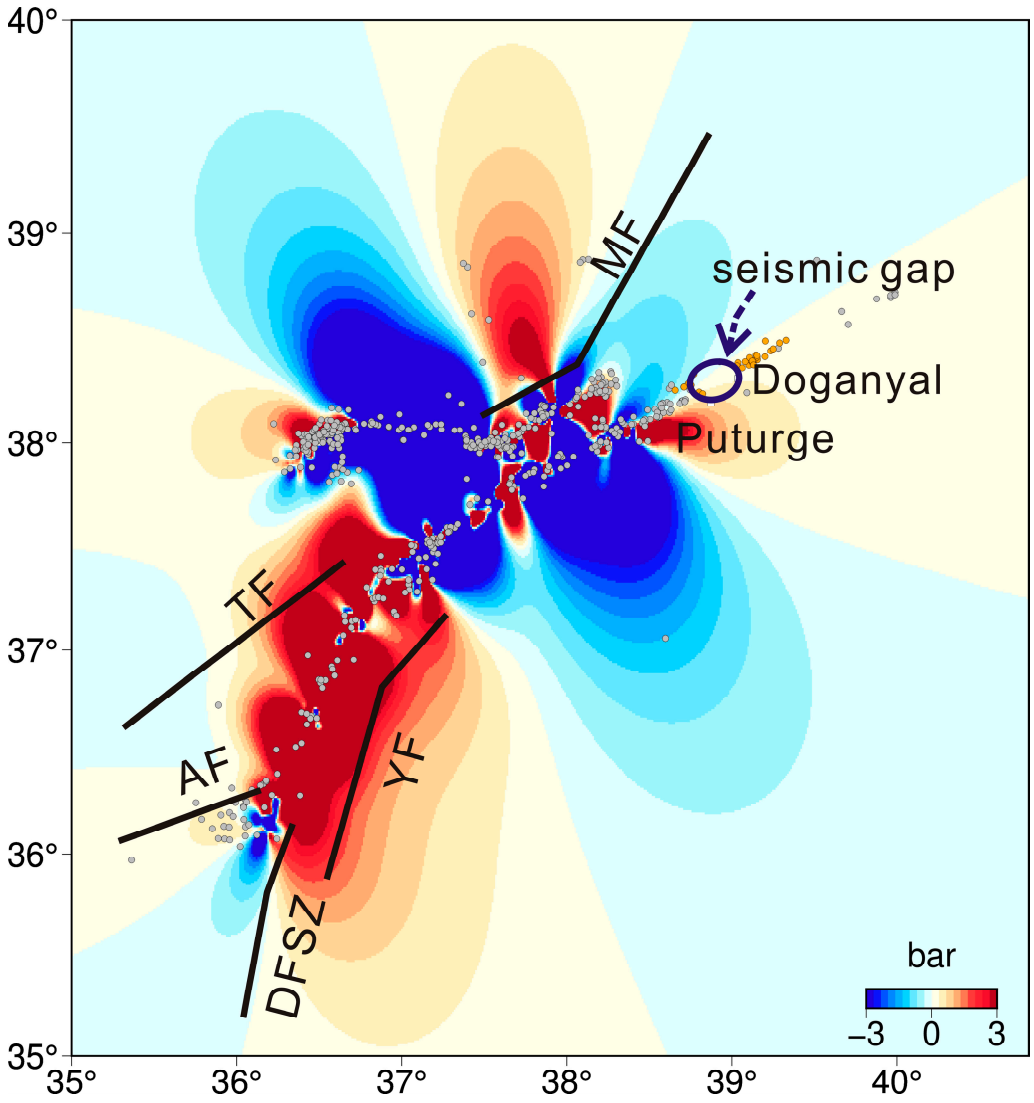

Figure 8. Coulomb failure stress (CFS) changes on surrounding faults of the 2023 Türkiye-Syria earthquake sequence. MF: Malatya Fault; TF: Turkoglu Fault; AF: Antakya Fault; YF: Yesemek Fault; DSFZ: Dead Sea Fault Zone. Grey circles denote aftershocks of the 2023 Turkey earthquake sequence (Mw > 4 within 3 months); orange circles denote aftershocks of the 2020 Turkey Mw 6.8 earthquake (Mw > 4).

4.3. Stress Perturbations in the Vicinity of the Türkiye-Syria Earthquake Sequence

Seismic gaps remain along the EAFZ following the Türkiye-Syria earthquake sequence [20,58]. Therefore, it is crucial to analyse the stress changes in the surrounding faults created by the seismic sequence. We simplified the geometry of the receiving fault by combining historical event source mechanisms and the fault strike. The receiver fault (strike = 277°, dip = 78°, rake = 4°) was based on the GCMT. According to the regional geological background and Coulomb stress research, we adopted $\mu = 0.4$ for the calculation. In the southwestern section of the Malatya Fault, the stress conditions displayed a cyclical pattern of alternating positive and negative states. The middle Puturge Fault, northern DSFZ, Yesemek Fault, Antakya Fault, and Turkoglu Fault are under strong positive stress and remain at high risk of large earthquakes (Figure 8).

By comparing the distribution of aftershocks (Mw > 4) following the 2023 earthquake sequence with that following the 2020 Mw 6.8 earthquake (orange circles in Figure 8), we found a moderately strong seismic gap along the west-central earthquake-prone Puturge Fault. The distribution of earthquakes is related to the inhomogeneity of the stress field. For

strain-expanding regions, there is mostly a normal rupture component, whereas the reverse component is mainly distributed in strain-compressed regions. From east to west along the Puturge Fault, the average dip gradually shallows from 70° to 40°. The corresponding strains are almost vertical in the east, gradually flatten out in the central-western area, and gradually change from horizontal to vertical near Gokdere. According to Bletery et al. [54], the maximum moment release was mainly concentrated on the east-west boundary curve of the Puturge Fault, which may be one reason why no major earthquakes have occurred along the middle-western Puturge Fault segment.

The aftershock sequence of the Türkiye-Syria earthquake doublet almost coincided with that of the 2020 Mw 6.8 earthquake on the Puturge segment. Additionally, studies have shown that nearly repetitive earthquakes occur throughout the region within 10 km along the Puturge segment [59]. This overlap may be associated with interseismic coupling [21]. Blettery et al. [54] showed that coupling is low along the eastern Puturge section but is high further west. The aftershock overlap zone is mainly in the transition zone between high and low coupling [60]. For small convex, partially or fully coupled faults, persistent creep-slip results in a uniform spatial distribution of earthquakes. As such, repeated areas of aftershocks also occur.

5. Conclusions

In this study, we utilised pixel offset tracking to record surface displacements resulting from the 2023 Türkiye-Syria earthquake sequence. Analysing these displacement changes provided insights into the geometric characteristics and deformation magnitudes of the fault ruptures. We then employed a homogeneous elastic half-space dislocation model to invert and map the distribution of coseismic slip during the earthquake sequence. Finally, we determined the dynamics of fault motion, rupture patterns, and stress transfer. The main conclusions are as follows: (1) The D-InSAR method faced challenges owing to near-surface incoherence, while SAR offset-tracking excelled at capturing near-field deformation details. (2) The cumulative deformation caused by the Mw 7.6 earthquake slightly exceeds that of the Mw 7.8 event. Furthermore, the ascending track displays slightly larger deformations compared with the descending track at the same location. (3) Both earthquakes predominantly exhibit left-lateral slip motion, with the depth of slip ranging from 0 to 20 km. Specifically, the Mw 7.8 earthquake mainly triggered slip in the east-central part of the southern EAFZ (S2 and S3), while the Mw 7.6 event induced slip concentrated on the western section of the northern EAFZ (S4). (4) The Mw 7.8 earthquake triggered the Mw 7.6 earthquake, while conversely, the Mw 7.6 earthquake strongly suppressed the central section (S2) of the southern branch of the EAFZ. (5) Following the Mw 7.6 earthquake, Coulomb stress is strongly loaded on the central Puturge Fault, northern DSFZ, Yesemek Fault, Antakya Fault, and Turkoglu Fault.

Author Contributions: Conceptualization, C.M. and Y.L.; methodology, W.W. and X.F.; validation, C.M., Y.L. and X.S.; formal analysis, W.W. and X.F.; investigation, Y.L. and X.F.; data curation, W.W.; writing-original draft preparation, W.W.; writing-review and editing, W.W. and X.F.; visualisation, W.W.; supervision, X.F.; project administration, Y.L.; funding acquisition, Y.L. and X.S. All authors have read and agreed to the published version of the manuscript.

Funding: This work was co-supported by Grants from the National Nonprofit Fundamental Research of Institute of Geology, China Earthquake Administration (Grant No. IGCEA2005) and the National Science Foundation of China (Grant No. 42274046, 41874027).

Data Availability Statement: The Sentinel-1 SAR data were acquired and processed by the European Space Agency Copernicus program (https://scihub.copernicus.eu/, accessed on 24 February 2023) and were retrieved from the Alaska Satellite Facility Distributed Active Archive Center (https://vertex.daac.asf.alaska.edu, accessed on 24 February 2023). The preliminary surface ruptures of the Turkey earthquake sequence based on analysis of post-seismic satellite data were obtained from USGS (https://usgs.maps.arcgis.com/apps/webappviewer/indexhtml?id=5229bb842bd64b688d769abbefe43b46, accessed on 26 March 2023). The relocated aftershocks of the 2023 Turkey

earthquake sequence were archived from Zenodo (https://zenodo.org/record/7699882#.ZEKnT3ZBy3A, accessed on 26 March 2023). The aftershocks of the 2020 Turkey earthquake sequence were archived from the AFAD catalog (https://deprem.afad.gov.tr/event-catalog, accessed on 26 March 2023).

Acknowledgments: We thank the editor and the three anonymous reviewers for their constructive suggestions that significantly improved the quality of the manuscript.

Conflicts of Interest: The authors declare no conflict of interest.

References

1. Mai, P.M.; Aspiotis, T.; Aquib, T.A.; Valero Cano, E.; Castro Cruz, D.A.; Espindola-Carmona, A.; Li, B.; Li, X.; Liu, J.; Matrau, R.; et al. The Destructive Earthquake Doublet of 6 February 2023 in South-Central Türkiye and Northwestern Syria: Initial Observations and Analyses. *Seism. Rec.* **2023**, *3*, 105–115. [CrossRef]
2. Emre, Ö.; Duman, T.Y.; Özalp, S.; Elmaci, H. *Active Fault Map of Turkey with an Explanatory Text 1: 1,250,000 Scale*; special publication series 30; General Directorate of Mineral Research and Exploration: Ankara, Turkey, 2013; p. 89.
3. Gülen, L.; Barka, A.; Toksöz, M.N. Continental collision and related complex deformation: Maras triple junction and surrounding structures, SE Turkey. *Hacet. Univ. Earth Sci. J.* **1987**, *14*, 319–336.
4. Barbot, S.; Weiss, J.R. Connecting subduction, extension and shear localization across the Aegean Sea and Anatolia. *Geophys. J. Int.* **2021**, *226*, 422–445. [CrossRef]
5. Melgar, D.; Taymaz, T.; Ganas, A.; Crowell, B.; Öcalan, T.; Kahraman, M.; Tsironi, V.; Yolsal-Çevikbilen, S.; Valkaniotis, S.; Irmak, T.S.; et al. Sub-and super-shear ruptures during the 2023 Mw 7.8 and Mw 7.6 earthquake doublet in SE Türkiye. *Seismica* **2023**, *2*. [CrossRef]
6. Zahradník, J.; Turhan, F.; Sokos, E.; Gallovič, F. Asperity-like (segmented) structure of the 6 February 2023 Turkish earthquakes. *Earth ArXiv* **2023**. [CrossRef]
7. Jiao, X.; Liu, C.; Xiong, X. Source process of the 24 January 2020 Mw 6.7 East Anatolian fault zone, Turkey, earthquake. *Seismol. Res. Lett.* **2020**, *91*, 3120–3128.
8. Lin, X.; Hao, J.; Wang, D.; Chu, R.; Zeng, X.; Xie, J.; Zhang, B.; Bai, Q. Coseismic Slip Distribution of the 24 January 2020 Mw 6.7 Doganyol Earthquake and in Relation to the Foreshock and Aftershock Activities. *Seism. Res. Lett.* **2020**, *92*, 127–139. [CrossRef]
9. Jia, Z.; Jin, Z.; Marchandon, M.; Ulrich, T.; Gabriel, A.-A.; Fan, W.; Shearer, P.; Zou, X.; Rekoske, J.; Bulut, F.; et al. The complex dynamics of the 2023 Kahramanmaraş, Turkey, Mw 7.8–7.7 earthquake doublet. *Science* **2023**, *381*, 985–990. [CrossRef]
10. Meng, L.; Xu, L.; Mohanna, S.; Ji, C.; Ampuero, J.; Yunjun, Z.; Hasnain, M.; Chu, R. The 2023 Mw7.8 Kahramanmaraş, Turkey Earthquake: A Multi-segment Rupture in A Mil-lennium Supercycle. *Res. Sq. pre-print*. [CrossRef]
11. Atanasova, M.; Raykova, P.; Nikolov, H. Determining the Deformations of the Earth's Surface after the Earthquakes in Turkey-Syria of 06 February 2023—Initial Results. *C. R. Acad. Bulg. Sci.* **2023**, *76*, 554–562. [CrossRef]
12. Li, S.; Wang, X.; Tao, T.; Zhu, Y.; Qu, X.; Li, Z.; Huang, J.; Song, S. Source Model of the 2023 Turkey Earthquake Sequence Imaged by Sentinel-1 and GPS Measurements: Implications for Heterogeneous Fault Behavior along the East Anatolian Fault Zone. *Remote Sens.* **2023**, *15*, 2618. [CrossRef]
13. An, Q.; Feng, G.; He, L.; Xiong, Z.; Lu, H.; Wang, X.; Wei, J. Three-Dimensional Deformation of the 2023 Turkey Mw 7.8 and Mw 7.7 Earthquake Sequence Obtained by Fusing Optical and SAR Images. *Remote Sens.* **2023**, *15*, 2656. [CrossRef]
14. Zhang, G.; Qu, C.; Shan, X.; Song, X.; Zhang, G.; Wang, C.; Hu, J.-C.; Wang, R. Slip distribution of the 2008 Wenchuan Ms 7.9 earthquake by joint inversion from GPS and InSAR measurements: A resolution test study. *Geophys. J. Int.* **2011**, *186*, 207–220. [CrossRef]
15. Reilinger, R.; McClusky, S. Nubia-Arabia-Eurasia plate motions and the dynamics of Mediterranean and Middle East tectonics. *Geophys. J. Int.* **2011**, *186*, 971–979. [CrossRef]
16. Sboras, S.; Lazos, I.; Bitharis, S.; Pikridas, C.; Galanakis, D.; Fotiou, A.; Chatzipetros, A.; Pavlides, S. Source model-ling and stress transfer scenarios of the October 30, 2020 Samos earthquake: Seismotectonic implications. *Turk. J. Earth Sci.* **2021**, *30*, 699–717. [CrossRef]
17. Jolivet, L.; Faccenna, C.; Huet, B.; Labrousse, L.; Le Pourhiet, L.; Lacombe, O.; Lecomte, E.; Burov, E.; Denèle, Y.; Brun, J.-P.; et al. Aegean tectonics: Strain localisation, slab tearing and trench retreat. *Tectonophysics* **2013**, *597*, 1–33. [CrossRef]
18. Faccenna, C.; Becker, T.W.; Auer, L.; Billi, A.; Boschi, L.; Brun, J.P.; Capitanio, F.A.; Funiciello, F.; Horvàth, F.; Jolivet, L.; et al. Mantle dynamics in the Mediterranean. *Rev. Geophys.* **2014**, *52*, 283–332. [CrossRef]
19. Gallovič, F.; Zahradník, J.; Plicka, V.; Sokos, E.; Evangelidis, C.; Fountoulakis, I.; Turhan, F. Complex rupture dynamics on an immature fault during the 2020 Mw 6.8 Elazığ earthquake, Turkey. *Commun. Earth Environ.* **2020**, *1*, 40. [CrossRef]
20. Duman, T.Y.; Ömer, E. *The East Anatolian Fault: Geometry, Segmentation and Jog Characteristics*; Geological Society; London, Special Publications: London, UK, 2013; Volume 372, pp. 495–529.
21. Güvercin, S.E.; Karabulut, H.; Konca, A.; Doğan, U.; Ergintav, S. Active seismotectonics of the East Anatolian Fault. *Geophys. J. Int.* **2022**, *230*, 50–69. [CrossRef]
22. Herece, E. *Doğu Anadolu Fayı (DAF) Atlası [East Anatolian Fault (EAF) Atlas]*; MTA: Ankara, Turket, 2008; Volume 359.

23. Reilinger, R.; McClusky, S.; Vernant, P.; Lawrence, S.; Ergintav, S.; Cakmak, R.; Ozener, H.; Kadirov, F.; Guliev, I.; Stepanyan, R.; et al. GPS constraints on continental deformation in the Africa-Arabia-Eurasia continental collision zone and implications for the dynamics of plate interactions. *J. Geophys. Res. Solid Earth* **2006**, *111*, B5. [CrossRef]
24. Aktug, B.; Ozener, H.; Dogru, A.; Sanbucu, A.; Turgut, B.; Halicioglu, K.; Yilmaz, O.; Havazli, E. Slip rates and seis-mic potential on the East Anatolian Fault System using an improved GPS velocity field. *J. Geod.* **2016**, *94–95*, 1–12.
25. Westaway, R.O.B.; Arger, J.A.N. The Gölbai basin, southeastern Turkey: A complex discontinuity in a major strike-slip fault zone. *J. Geol. Soc.* **1996**, *153*, 729–744. [CrossRef]
26. Karabacak, V.; Yönlü, Ö.; Altunel, E.; Yalçıner, C.Ç.; Akyüz, H.S.; Kıyak, N.G. Doğu Anadolu Fay Zonu güneybatı uzanımının paleosismolojisi ve ilk kayma hızı bulguları. In *ATAG-15 (Aktif Tektonik Araştırma Grubu 15. Çalıştayı) Bildiri Özleri Kitabı*; Çukurova Üniversitesi: Adana, Turkey, 2011.
27. Lomax, A. Precise, NLL-SSST-Coherence Hypocenter Catalog for the 2023 Mw 7.8 and Mw 7.6 SE Turkey Earthquake Sequence. Zenodo. 2023. Available online: https://zenodo.org/records/7727678 (accessed on 20 October 2023).
28. Armijo, R.; Meyer, B.; Hubert, A.; Barka, A. Westward propagation of the North Anatolian fault into the northern Aegean: Timing and kinematics. *Geology* **1999**, *27*, 267–270. [CrossRef]
29. Hu, J.; Liu, J.; Li, Z.; Zhu, J.; Wu, L.; Sun, Q.; Wu, W. Estimating threedimensional coseismic deformations with the SM-VCE method based on heterogeneous SAR observations: Selection of homogeneous points and analysis of observation combinations. *Remote Sens. Environ.* **2021**, *255*, 112298. [CrossRef]
30. Liu, J.; Hu, J.; Li, Z.; Ma, Z.; Wu, L.; Jiang, W.; Feng, G.; Zhu, J. Complete three-dimensional coseismic displacements due to the 2021 Maduo earthquake in Qing-hai Province, China from Sentinel-1 and ALOS-2 SAR images. *Sci. China Earth Sci.* **2022**, *65*, 687–697. [CrossRef]
31. Bürgmann, R.; Schmidt, D.; Nadeau, R.M.; D'Alessio, M.; Fielding, E.; Manaker, D.; McEvilly, T.V.; Murray, M.H. Earthquake Potential Along the Northern Hayward Fault, California. *Science* **2000**, *289*, 1178–1182. [CrossRef]
32. Li, Y.; Bürgmann, R. Partial Coupling and Earthquake Potential Along the Xianshuihe Fault, China. *J. Geophys. Res. Solid Earth* **2021**, *126*, e21406. [CrossRef]
33. Gabriel, A.K.; Goldstein, R.M.; Zebker, H.A. Mapping small elevation changes over large areas: Differential radar inter-ferometry. *J. Geophys. Res.* **1989**, *94*, 9183–9191. [CrossRef]
34. Shan, X.-J.; Qu, C.-Y.; Gong, W.-Y.; Zhao, D.-Z.; Zhang, Y.-F.; Zhang, G.-H.; Song, X.-G.; Liu, Y.-H.; Zhang, G.-F. Coseismic deformation field of the Jiuzhaigou MS7.0 earthquake from Sentinel-1A InSAR data and fault slip inversion. *Chin. J. Geophys.* **2017**, *60*, 4527–4536. (In Chinese)
35. Zhao, D.; Qu, C.; Bürgmann, R.; Gong, W.; Shan, X. Relaxation of Tibetan Lower Crust and Afterslip Driven by the 2001 Mw7.8 Kokoxili, China, Earthquake Constrained by a Decade of Geodetic Measurements. *J. Geophys. Res. Solid Earth* **2021**, *126*, e2020JB021314. [CrossRef]
36. Fan, X.; Zhang, G.; Zhao, D.; Xie, C.; Huang, C.; Shan, X. Fault geometry and kinematics of the 2021 Mw 7.3 Maduo earthquake from aftershocks and InSAR observations. *Front. Earth Sci.* **2022**, *10*, 993984. [CrossRef]
37. Chen, H.; Qu, C.; Zhao, D.; Ma, C.; Shan, X. Rupture Kinematics and Coseismic Slip Model of the 2021 Mw 7.3 Maduo (China) Earthquake: Implications for the Seismic Hazard of the Kunlun Fault. *Remote Sens.* **2021**, *13*, 3327. [CrossRef]
38. Michel, R.; Avouac, J.-P.; Taboury, J. Measuring ground displacements from SAR amplitude images: Application to the Landers Earthquake. *Geophys. Res. Lett.* **1999**, *26*, 875–878. [CrossRef]
39. Wang, L.; Deng, K.; Zheng, M. Research on ground deformation monitoring method in mining areas using the probability integral model fusion D-InSAR, sub-band InSAR and offset-tracking. *Int. J. Appl. Earth Obs. Geoinf.* **2020**, *85*, 101981. [CrossRef]
40. Fan, H.; Gao, X.; Yang, J.; Deng, K.; Yu, Y. Monitoring Mining Subsidence Using A Combination of Phase-Stacking and Off-set-Tracking Methods. *Remote Sens.* **2015**, *7*, 9166–9183. [CrossRef]
41. Werner, C.; Wegmüller, U.; Strozzi, T.; Wiesmann, A. Gamma SAR and interferometric processing software. In Proceedings of the Ersenvisat Symposium, Gothenburg, Sweden, 16–20 October 2000; Volume 1620.
42. Goldstein, R.M.; Werner, C.L. Radar interferogram filtering for geophysical applications. *Geophys. Res. Lett.* **1998**, *25*, 4035–4038. [CrossRef]
43. Lo, R.W.; Levitt, K.N.; Olsson, R.A. MCF: A malicious code filter. *Comput. Secur.* **1995**, *14*, 541–566. [CrossRef]
44. Zhao, D.; Qu, C.; Shan, X.; Gong, W.; Zhang, Y.; Zhang, G. InSAR and GPS derived coseismic deformation and fault model of the 2017 Ms7. 0 Jiuzhaigou earthquake in the Northeast Bayanhar block. *Tectonophysics* **2018**, *726*, 86–99. [CrossRef]
45. Li, Z.; Song, G.; Yu, C.; Xiao, R.; Chen, L.; Luo, H.; Dai, K.; Ge, D.; Ding, Y.; Zhang, Y.; et al. Application of satellite radar remote sensing in landslide disaster detection and monitoring: Challenges and countermeasures. *J. Wuhan Univ. (Inf. Sci. Ed.)* **2019**, *44*, 967–979. [CrossRef]
46. Rott, H.; Stuefer, M.; Siegel, A.; Skvarca, P.; Eckstaller, A. Mass fluxes and dynamics of Moreno Glacier, Southern Patagonia Icefield. *Geophys. Res. Lett.* **1998**, *25*, 1407–1410. [CrossRef]
47. Gray, A.; Short, N.; Mattar, K.; Jezek, K. Velocities and Flux of the Filchner Ice Shelf and its Tributaries Determined from Speckle Tracking Interferometry. *Can. J. Remote Sens.* **2001**, *27*, 193–206. [CrossRef]
48. Liu, Y.; Qu, C.; San, X. Obtaining two-dimensional deformation field of Wenchuan earthquake based on SAR image offset. *J. Geophys.* **2012**, *55*, 3296–3306.

49. Strozzi, T.; Luckman, A.; Murray, T.; Wegmuller, U.; Werner, C. Glacier motion estimation using sar offset-tracking procedures. *IEEE Trans. Geosci. Remote Sens.* **2002**, *40*, 2384–2391. [CrossRef]
50. Feng, G.; Li, Z.; Shan, X.; Zhang, L.; Zhang, G.; Zhu, J. Geodetic model of the 2015 April 25 Mw 7.8 Gorkha Nepal Earthquake and Mw 7.3 aftershock estimated from InSAR and GPS data. *Geophys. J. Int.* **2015**, *203*, 896–900. [CrossRef]
51. Corzo, G.; Varouchakis, E.A. (Eds.) *Spatiotemporal Analysis of Extreme Hydrological Events*; Elsevier: Amsterdam, The Netherlands, 2018.
52. Wang, R.; Parolai, S.; Ge, M.; Jin, M.; Walter, T.R.; Zschau, J. The 2011 Mw 9.0 Tohoku Earthquake: Comparison of GPS and Strong-Motion Data. *Bull. Seism. Soc. Am.* **2013**, *103*, 1336–1347. [CrossRef]
53. Okada, Y. Surface deformation due to shear and tensile faults in a half-space. *Bull. Seism. Soc. Am.* **1985**, *75*, 1135–1154. [CrossRef]
54. Bletery, Q.; Cavalié, O.; Nocquet, J.; Ragon, T. Distribution of Interseismic Coupling Along the North and East Anatolian Faults Inferred from InSAR and GPS Data. *Geophys. Res. Lett.* **2020**, *47*, e2020GL087775. [CrossRef]
55. Harris, R.A. Introduction to Special Section: Stress Triggers, Stress Shadows, and Implications for Seismic Hazard. *J. Geophys. Res. Solid Earth* **1998**, *103*, 24347–24358. [CrossRef]
56. Shan, X.; Li, Y.; Gao, Z.; Hua, J.; Huang, X.; Gong, W.; Qu, C.; Zhao, D.; Chen, J.; Huang, C.; et al. Co-seismic deformation characteristics of the 2022 Luding M_S6.8 earthquake and the risk of strong earthquakes in the vicinity. *Sci. Bull.* **2023**, *68*, 944–953.
57. Harris, R.A.; Simpson, R.W. In the shadow of 1857—The effectof the great Ft. Tejon earthquake on subsequent earthquakes insouthern California. *Geophys. Res. Lett.* **1996**, *23*, 229–232. [CrossRef]
58. Gülerce, Z.; Shah, S.T.; Menekşe, A.; Özacar, A.A.; Kaymakci, N.; Çetin, K. Probabilistic Seismic-Hazard Assessment for East Anatolian Fault Zone Using Planar Fault Source Models. *Bull. Seism. Soc. Am.* **2017**, *107*, 2353–2366. [CrossRef]
59. Konca, A.Ö.; Karabulut, H.; Güvercin, S.E.; Eskiköy, F.; Özarpacı, S.; Özdemir, A.; Floyd, M.; Ergintav, S.; Doğan, U. From Interseismic Deformation with Near-Repeating Earthquakes to Co-Seismic Rupture: A Unified View of the 2020 Mw6. 8 Sivrice (Elazığ) Eastern Turkey Earthquake. *J. Geophys. Res. Solid Earth* **2021**, *126*, e2021JB021830. [CrossRef]
60. Metois, M.; Vigny, C.; Socquet, A. Interseismic coupling, megathrust earthquakes and seismic swarms along the Chilean subduction zone (38–18 S). *Pure Appl. Geophys.* **2016**, *173*, 1431–1449. [CrossRef]